

# Spectral diagnosis of wire arc additive manufacturing of Al alloys

Chen Zhang<sup>a</sup>, Ming Gao<sup>b,\*</sup>, Cong Chen<sup>b</sup>, Xiaoyan Zeng<sup>b</sup>

<sup>a</sup> The Institute of Technological Sciences, Wuhan University, Wuhan, 430072, PR China

<sup>b</sup> Wuhan National Laboratory for Optoelectronics, Huazhong University of Science and Technology, Wuhan, 430074, PR China

## ARTICLE INFO

### Keywords:

Additive manufacturing  
Spectral diagnosis  
Porosity  
Microstructures  
Forming size

## ABSTRACT

Online nondestructive testing for quality control is a critical direction for research in additive manufacturing in the future. In this study, for the first time, optical emission spectroscopy was employed to probe the arc characteristics in the wire arc additive manufacturing (WAAM) of an Al alloy and to detect its structural features. The arc characteristics, such as spectral intensity, electron density, and electron temperature, were calculated based on the atomic emission spectral lines. The resulting structural features of the deposited layers, namely the forming width, composition, grain size, and porosity defects, were analyzed, and a correlation between the arc characteristics and the structural features was proposed. The arc cathode size, which changed with the number of deposited layers, controlled the arc energy distribution. Hence, the forming width had an approximately linear relation with the spectral intensity of Mg (a constituent of the alloy used for the wire feed) and the electron density. The porosity in the alloy was observed to be caused by H, which was a dominant pollutant in the process. Furthermore, the correlation between the porosity and H spectral intensity was observed to be approximately linear. However, no significant correlation between the grain size and the spectrum was noticeable. The results from this study establish the applicability of spectral diagnosis of the forming size and the porosity in WAAM.

## 1. Introduction

Wire arc additive manufacturing (WAAM) has high deposition efficiency and is ideal for manufacturing large and complex aluminum (Al) alloy parts [1,2]. However, inhomogeneous microstructures, porosity, and low accuracy of forming dimensions often occur in WAAM of Al alloys. The inadequate quality and lack of repeatability of WAAM significantly limits its application. To improve the quality and repeatability of WAAM, process monitoring and real-time process control are the need of the hour [3–7].

Thermographic and visual monitoring methods were commonly used to enhance the quality and repeatability of additive manufacturing in earlier studies [8–11]. For example, Clijsters et al. [12] developed a system with a data processing algorithm, and used a planar photodiode and a high-speed complementary metal-oxide-semiconductor (CMOS) camera to identify material discontinuities caused by the process failure, and to monitor the powder bed. Hua et al. [13] showed that pyrometry data could be used to correlate the melt pool size and the layer thickness during the directed energy deposition (DED) of powder. Rodriguez et al. [14] found that the defects caused by “over-melting” during the electron beam powder bed fusion could be identified through infrared imaging. Song et al. [15] presented a hybrid control

system to improve the dimensional accuracy in DED, which included a triangular-shaped configuration of three high-speed charge-couple device (CCD) cameras for monitoring the melt pool height, and a dual-color pyrometer for monitoring the melt pool temperature. It is evident from the above studies that the thermographic and visual monitoring methods mainly detect the structure of the surface layer, rather than the internal structures. However, detecting the internal structure is considered more critical, in view of its influence on the performance of WAAM.

Recently, some more new methods have been studied to inspect the additive manufacturing process. Watkins et al. [16] used neutron diffraction to detect the residual strains and stresses for wire-DED and laser powder bed fusion (laser-PBF). They also compared results from X-ray computed tomography (CT) with those from neutron CT and pointed out that the penetration depth of the neutrons was better than that of the X-rays. Cunningham et al. [17] used ultra-high-speed synchrotron X-ray imaging to quantify the keyhole pore formation during laser-PBF [17]. They found that the processing parameters and the keyhole shape were correlated, and that the parameters could be tuned to mitigate the pore formation. Laser ultrasonics is another technique that can be used on additive manufacturing components [18]. However, there has not been much research on the WAAM online detection

\* Corresponding author.

E-mail address: [mgao@mail.hust.edu.cn](mailto:mgao@mail.hust.edu.cn) (M. Gao).

<https://doi.org/10.1016/j.addma.2019.100869>

Received 16 June 2019; Received in revised form 8 September 2019; Accepted 10 September 2019

Available online 19 September 2019

2214-8604/ © 2019 Elsevier B.V. All rights reserved.

technology. The methods mentioned previously are difficult to apply to online detection of the WAAM process. This is because the WAAM process involves an extremely strong wide-band arc light and high decibels of noise, which would interfere with the camera sensor, ultrasonic probe, X-ray probe, and other probing equipment. Therefore, the detection accuracy is not guaranteed. Xiong et al. [19] designed a computer vision-sensing system that used a complex composite filtering technique to overcome this issue. They extracted the widths of the deposited layers successfully under a strong arc light. However, it was not sufficient to capture the surface widths accurately. Furthermore, detecting the internal structures, which is very critical, was not considered by them.

Arc characteristics have a significant influence on the forming size and the microstructures in arc welding [20]. In addition, they are influenced by the external electromagnetic environment. For example, the electrode offset and the workpiece edge welding can easily cause a magnetic blow, which leads to an asymmetrical arc, which in turn, affects the shape and the size of the weld [21,22]. The arc shape determines the energy distribution inside the arc. Thus, the asymmetric heat input due to the asymmetric arc results in uneven microstructures. In the WAAM of single-bead multi-layer parts, the arc usually starts depositing on a large substrate, which is similar to bead-on-plate welding. Then, the arc works mostly at the edge of the parts, which is similar to workpiece edge welding. Thus, carrying out online measurement of the arc characteristics may help us evaluate the forming size and the microstructures of the WAAM of Al alloys.

Stutzman et al. [23] utilized optical emission spectroscopy and plume imaging to investigate the flaws produced in DED processing, and revealed that the flaw density increased with an increase in the median line-to-continuum ratio to around 430–520 nm, and an increase in the total plume area. Their excellent work inspired the current authors to consider the possibility of using optical emission spectroscopy for the diagnosis of WAAM. The optical emission spectroscopy detection method, with features, such as long working distance, non-contact, and immunity to high brightness of light, can diagnose the electrical arc effectively. In fact, this method has been successfully applied in analyzing arc welding [24–26]. In addition, the mechanical properties of the welds can also be evaluated by this method [27,28]. As WAAM evolved from arc welding, optical spectroscopy is suitable for detecting the arc characteristics of WAAM as well. This study specifically conducts spectral analysis of the arc characteristics, and based on the same, analyzes the porosity, forming size, and grain size on different deposited layers. Thus, the ultimate objective of this study is to find a correlation between the arc characteristics and the structural features.

## 2. Experimental methods

### 2.1. Experimental setup and sample fabrication

Fig. 1a shows the experimental setup that comprised a Fanuc 710i robotic arm, a Fronius cold metal transfer (CMT) welder, an Andor ME5000 spectrometer with an iStar iCCD, and a Panasonic HC camera. The spectrometer had a wavelength range of 200–950 nm and a resolution,  $\lambda/\Delta\lambda$ , of 5000. The exposure time of the spectrometer was 150 ms. The spectrometer was calibrated using a standard mercury lamp supplied by the manufacturer before collecting the data. An optical fiber with a core diameter of 50  $\mu\text{m}$  was used to couple the light source to the spectrometer. The light collector consisted of a 75% optical attenuator and a 1 mm aperture. The center lines of the collector and the camera lens both passed through the center of the arc at a horizontal location 2 mm above the substrate surface. The head of the collector was 200 mm away from the central arc. A welding protective lens was placed before the camera lens. The camera was located 500 mm away from the central arc. The feedstock wire was made of Al-6.12Mg-0.48Mn-0.23Si-0.18Ti (Wt.%) alloy and had a diameter of 1.2 mm. The substrate with a thickness of 10 mm was made of pure Al.

The shielding gas was 99.9% argon with a flow rate of 25 L/min.

During the manufacturing process, the robotic arm moved the welding torch to build multilayered thin wall parts on the substrates. The moving torch for each layer had the same motion/direction vector. Each sample contained 15 layers and had a length of 100 mm at least. The robotic arm and the welder paused for 300 s before depositing the next layer so that the deposited layer could cool down to the ambient temperature, and thus avoid heat accumulation. The spectrometer and the camera collected the data simultaneously during the process.

Table 1 shows the processing parameters. Every single deposited layer of each sample was manufactured with the same parameters. It can be observed that the wire feeding speed, current, and voltage have significant influence on the forming size and the microstructures. The control software of the welder worked in a unified parameter adjustment mode. Therefore, the current was taken as the main variable in this study. The wire feeding speed and the voltage automatically changed with the current. The current was in the CMT pulse mode and the waveform of the pulse is shown in Fig. 1b. The current and voltage for different samples shown in Table 1 were the averages of the pulse waveform. The average current and voltage of the arc were maintained constant for every deposited layer in each sample. Hence, in all the subsequent discussions, the term current refers to the average current.

### 2.2. Forming size and microstructures

The width of the deposited layer ( $W$ ) was measured by analyzing the cross-section of the macroscopic metallographic samples. The metallographic samples were cut by using a wire cut electrical discharge machining. Then the metallographic samples were ground with a grinding paper and finally polished using  $\text{Al}_2\text{O}_3$ . The microstructures were characterized by a scanning electron microscope (SEM). The elemental compositions of different deposited layers were analyzed by an energy dispersive spectroscope (EDS), and the crystal structures of the metallographic samples, by electron backscatter diffraction (EBSD). The samples were electropolished with 90% perchloric acid and 10% absolute ethyl alcohol for 20 s and the micro-hardness of the samples was measured by Vickers hardness tester. The micro-hardness was measured at 10 test points on the chosen deposited layer. The test locations for EDS, EBSD, and micro-hardness are shown in Fig. 1c.

### 2.3. Porosity detection

The pore defects in the melting process of the aluminum alloy result from hydrogen in the pollutant. The higher the content of hydrogen in the pollutant, the higher the porosity. For this reason, in this study, organic pollutants with pre-determined amounts were introduced in the middle of the deposited layers to produce different percentages of porosity. Lubricating oil has been used as the pollutant, and the pre-coated position was within a width range of 2 mm at the middle of the deposited layer. The parameters are shown in Table 1. Metallographic micrograph, which is a reliable and low cost method for local pore analysis, was used for porosity evaluation. The percent porosity is the ratio of the total pore area to the total sectional area on a longitudinal section of the center deposited layer. The processing method of the metallographic samples is the same as in macroscopic metallography. To verify whether the porosity of the metallographic micrograph was accurate, the porosity of a representative sample from the metallographic micrograph was compared to the result from the X-ray CT scanning analysis. The theoretical resolution of the X-ray microfocus CT equipment from Aolong Company was 5  $\mu\text{m}$ .

### 2.4. Analysis methods of spectroscopy

The atomic emission lines of each deposited layer were analyzed. The data in the stable segment of the arc were selected as valid data for the analysis. The iterative discrete wavelet transform was performed to

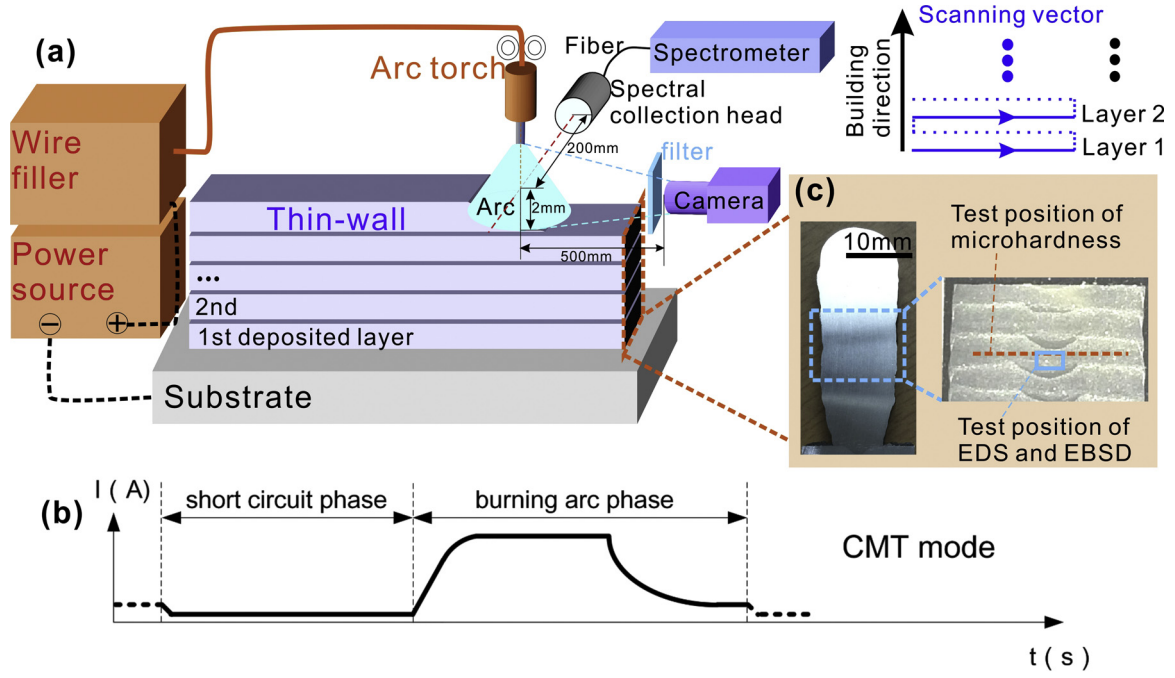


Fig. 1. (a) Schematic setup of spectral diagnosis in the WAAM process; (b) current waveform of the arc; (c) test locations on the cross section of the WAAM part.

Table 1

Processing parameters.

No.	Average current (A)	Average voltage (V)	Average wire filling speed (m/min)	Precoated contaminant weight (g)	Scanning speed (mm/s)
1	130	14.6	6.1	–	10
2	140	15.6	6.4	–	10
3	150	16.3	6.7	–	10
4	160	16.9	7.1	–	10
5	120	14.6	5.8	0	10
6	120	14.6	5.8	0.006	10
7	120	14.6	5.8	0.018	10
8	120	14.6	5.8	0.043	10

deduct the background noise of the spectral lines [29]. High intensity and high signal-noise ratio made the line Mg I 517.268 nm suitable for characterizing the spectral intensity ( $I_s$ ) of the arc as shown in Fig. 2a. The line Al I 396.152 nm with a high resolution has a weak self-absorption effect which is characterized by a sharp wave peak as shown in Fig. 2b. It was used to calculate the electron density ( $N_e$ ) of the arc by the Stark broadening method [30]:

$$N_e = \frac{\Delta\lambda_{\text{stark}}}{2\delta} \times 10^{22} \quad (1)$$

where,  $\Delta\lambda_{\text{stark}}$  is the full-width at half-maximum that can be obtained by Lorentz line shape fitting of spectral line Al I 396.152 nm; and  $\delta$  is electron collision broadening half-width that can be found in the extensive tables in [31]. Two Mg II ionic lines in 277–279 nm band, whose

wavelength spacing is short enough, were used to calculate the electron temperature ( $T_e$ ) of the arc. The electron temperature was calculated by the Boltzmann plot method in local thermodynamic equilibrium [32] [33].

$$\ln \frac{I_{ij}}{g_i A_{ij}} = -\frac{E_i}{kT_e} + \ln \frac{N^S}{U_S(T)} \quad (2)$$

With

$$x = E_i \quad (3)$$

$$y = \ln \frac{I_{ij}}{g_i A_{ij}} \quad (4)$$

Where,  $I_{ij}$  is the spectral intensity;  $g_i$  is the upper level degeneracy;  $A_{ij}$  is the transition probability;  $E_i$  is the upper level energy;  $k$  is the Boltzmann constant;  $N^S$  is the total particle number; and  $U_S(T)$  is the partition function. The  $x$  and  $y$  values can be calculated using the parameters in Table 2 and the measured spectral line intensities. The slope value  $m = -1/kT_e$  of the  $y=f(x)$  function can be obtained by linear fitting. Then,  $T_e$  would be equal to  $-1/(km)$ . The results were obtained by averaging the measured values of the five samples.

The porosity was detected by measuring the atomic emission lines of the polluted deposited layer. As the pore was closely related to the hydrogen content, the H I 656.28 nm spectral line, which had the highest intensity and a weak self-absorption effect (featured with a sharp wave peak as shown in Fig. 2c), was adopted to quantify the porosity. Spectral lines of different positions in the deposited layer with pre-coated contaminants were measured and analyzed.

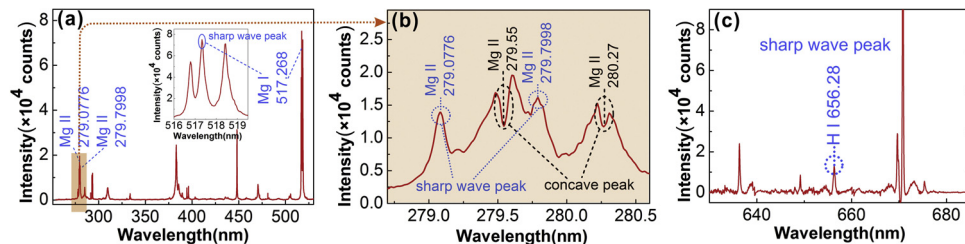
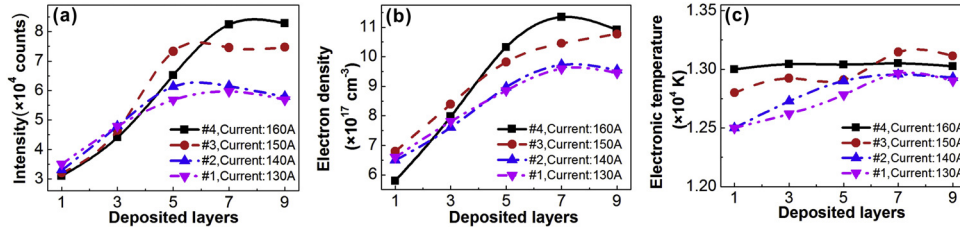


Fig. 2. (a) Spectral lines between wavelengths 250 and 550 nm; (b) locally amplified spectral lines in (a); (c) spectral lines between wavelengths 635 and 685 nm.

**Table 2**

The spectral line parameters for calculating electron temperature.

Atom/ion	Wavelength $\lambda$ (nm)	Upper level energy $E_i$ (eV)	Upper level degeneracy $g_i$	Transition probability $A_{ij}$ ( $s^{-1}$ )
Mg II	279.0776	8.8637	4	$4.01 \times 10^8$
Mg II	279.7998	8.8636	6	$4.79 \times 10^8$

**Fig. 3.** Arc characteristics as functions of the number of deposited layers; (a) spectral intensity; (b) electron density; (c) electron temperature.

### 3. Results and discussion

#### 3.1. Spectral characteristics of the arc in different deposited layers

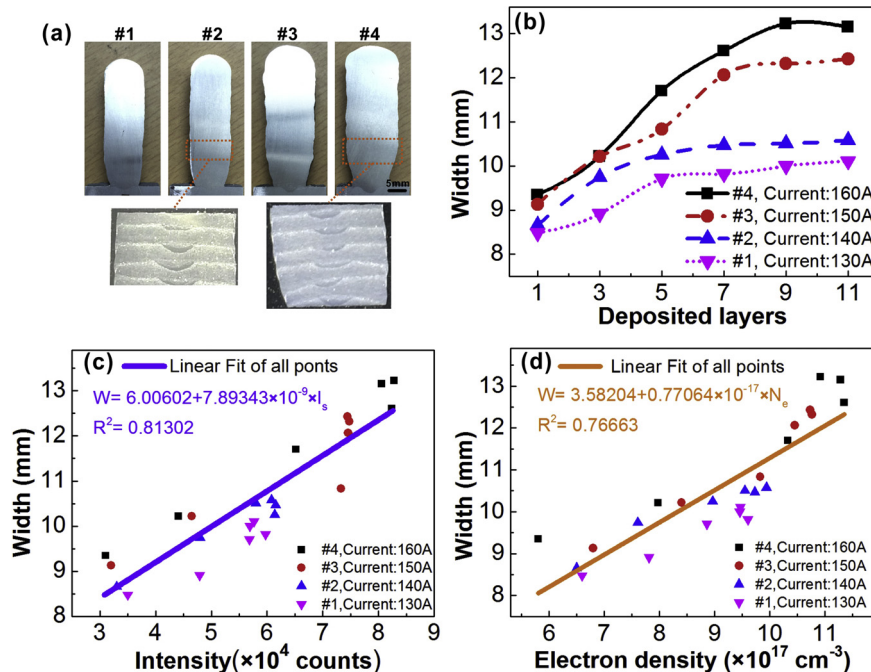
The effect of the number of deposited layers on the physical characteristics of the arc plume is shown in Fig. 3. The spectral intensity and the electron density of all the samples increased when the number of deposited layers increased. After the number of layers become 5–7, the spectral intensity and the electron density tended to be stable. Increasing the arc current increased the spectral intensity and the electron density in the stable stage. The electron temperature of samples #1 and #2 increased with the number of layers, while those of samples #3 and #4 did not as such.

#### 3.2. Relationship between the spectral characteristics of the arc and the forming size

The main forming features of the deposited layer were the height and the width. The metallography of cross sections for samples 1–4 is shown in Fig. 4a. As the number of deposited layers increased, the

height of the deposited layer did not change significantly. However, the width of the deposited layer accordingly became wider as shown in Fig. 4b. After the number of deposited layer reached to 5–7, the width tended to be stable. In the stable section, the larger average current made the deposited layer wider. This variation was similar to that of spectral intensity and electron density. Therefore, the forming width is correlated to the spectral intensity and the electron density of the arc. As shown in Fig. 4c and d, the width of all the samples increased with the spectral intensity and the electron density. Regression analyses between the arc characteristics and the width (W) of the deposited layers showed a good fitting result. This result proved that detecting the forming width by spectra measurement was feasible.

It is well known that the width of the deposited layer is determined by the arc energy distribution and the heat transfer process. In addition, the spectral characteristics of the arc are related to the particle density and the degree of ionization inside the arc. This leads to a question of whether there is a physical relation between the forming width and the arc characteristics. Exploring this question is helpful to understand the physical meaning of the curves in Fig. 4. Fig. 5a shows that the shape of the arc gradually changed from triangular at the first layer to a bell

**Fig. 4.** (a) Metallography of the cross section of the thin-walled samples; (b) the width of different deposited layers; (c) regression plots for the spectral intensity and the width of the deposited layers; (d) regression plots for the electron density and the width of the deposited layers.



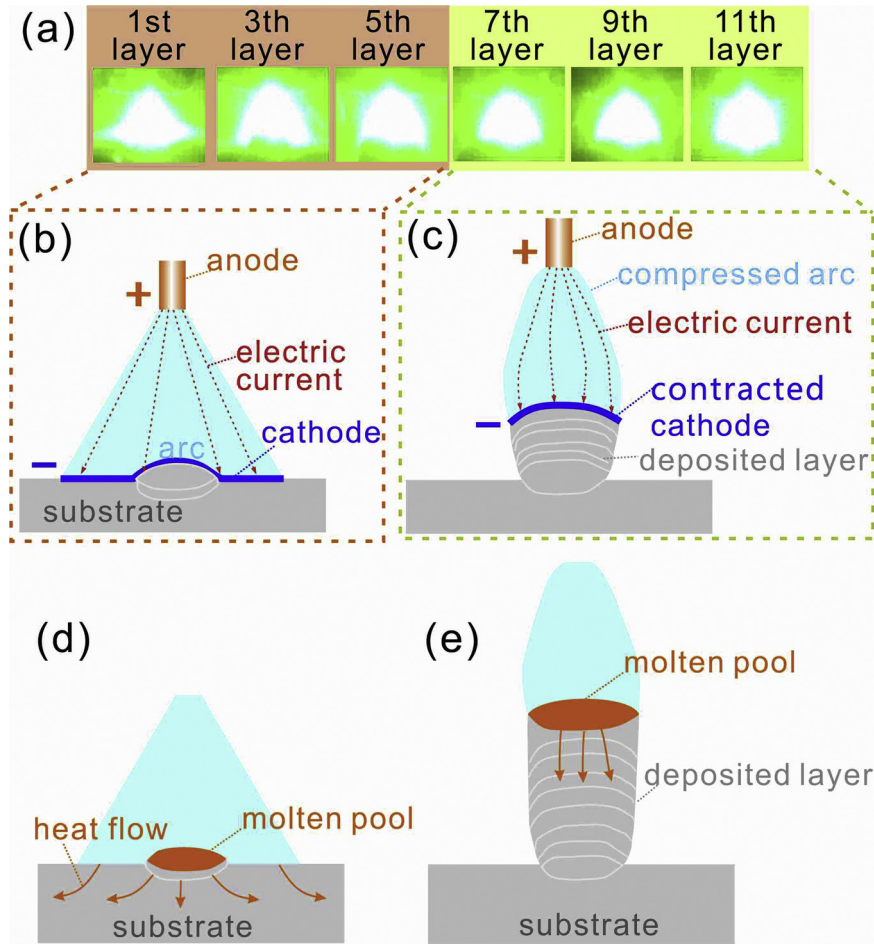


**Fig. 5.** (a) Arc shapes of different deposited layers; (b) and (c) illustration of the forming mechanism of different arc shapes; (d) energy transfer into the substrate in the initial deposited layers; (e) energy concentration in the upper deposited layer.

shape as the number of deposited layers increased. This indicates a volume compression of the cathode of the arc. The surface of the substrate was the cathode when the number of layer was less than 5 as shown in Fig. 5b and c. After the number of layers increased to more than 7, only the top surface of the thin wall acted as the cathode. The arc electric current density increased due to the smaller cathode area while the current and the voltage of the arc remain unchanged. The rising current density enhanced the electric field intensity near the cathode, which in turn, increased the number of emitted electrons per unit cathode surface area. This could be explained by the fact that the electron emission of the cathode during arc welding was mainly based on the field emission [34]. Thus, the compressed current arc and the enhanced cathode field emission together increased  $N_e$ . The increase in  $N_e$  enhanced the collision probability of neutral particles [35], which increased the arc ionization rate ( $\eta$ ). This increase in the ionization rate caused more photons to be radiated externally and enhanced  $I_s$ . The relationship between  $\eta$  and  $T_e$  can be obtained by the Saha equation [36] as follows:

$$\frac{\eta^2}{1 - \eta^2} = \left( \frac{2\pi m_e}{h^2} \right)^{3/2} \frac{(kT_e)^{5/2}}{p} \exp\left(-\frac{eV_i}{kT_e}\right) \quad (5)$$

Where,  $p$  is the gas pressure,  $V_i$  is the ionization voltage,  $e$  is the electron charge,  $m_e$  is the electron mass,  $h$  is the Planck constant, and  $k$  is the Boltzmann constant. This equation indicates that  $T_e$  increases as  $\eta$  increases. The above physical relation indirectly explains that the forming width has a good linear correspondence with the arc characteristics.

### 3.3. Relationship between the spectral characteristics of the arc and the microstructures

Fig. 6a–f show the element contents and the inverse pole figures in different deposited layers of sample #1. The elements at different layers were uniformly distributed, and all the grains were equiaxed with random orientations. Fig. 6g shows the statistics of the corresponding grain sizes. The coarse grains appeared in the upper part of the samples. The finer grain size led to an increase in micro-hardness, according to the Hall-Patch relationship as shown in Fig. 6g. The grain size increased with the increase in the arc characteristics, as shown in Fig. 6h. However, the fitting result between the grain size and the arc characteristics was not as evident as the relation between the width of the deposited layers and the arc characteristics. The correlation between micro-hardness and the spectrum was even weaker owing to the weak correlation between the microstructure and the spectrum.

The arc characteristics are some of the prominent factors that could influence the grain size. Some of the energy carried by the increased photons was transferred to the cathode by radiation. When the arc current in an Ar atmosphere was higher than 10 A,  $T_e$  was approximately equal to the thermodynamic temperature [37]. An increase in  $T_e$  was an indication that the thermodynamic temperature of the arc rose simultaneously and more heat was transferred to the cathode. These two heat transfer phenomena caused the cathode to absorb more energy from the arc in spite of the constant heat input of the welding power source. The increase in the arc characteristics meant higher absorbed energy. The increasing absorbed energy may have increased the grain size. However, a large amount of energy was transferred into the

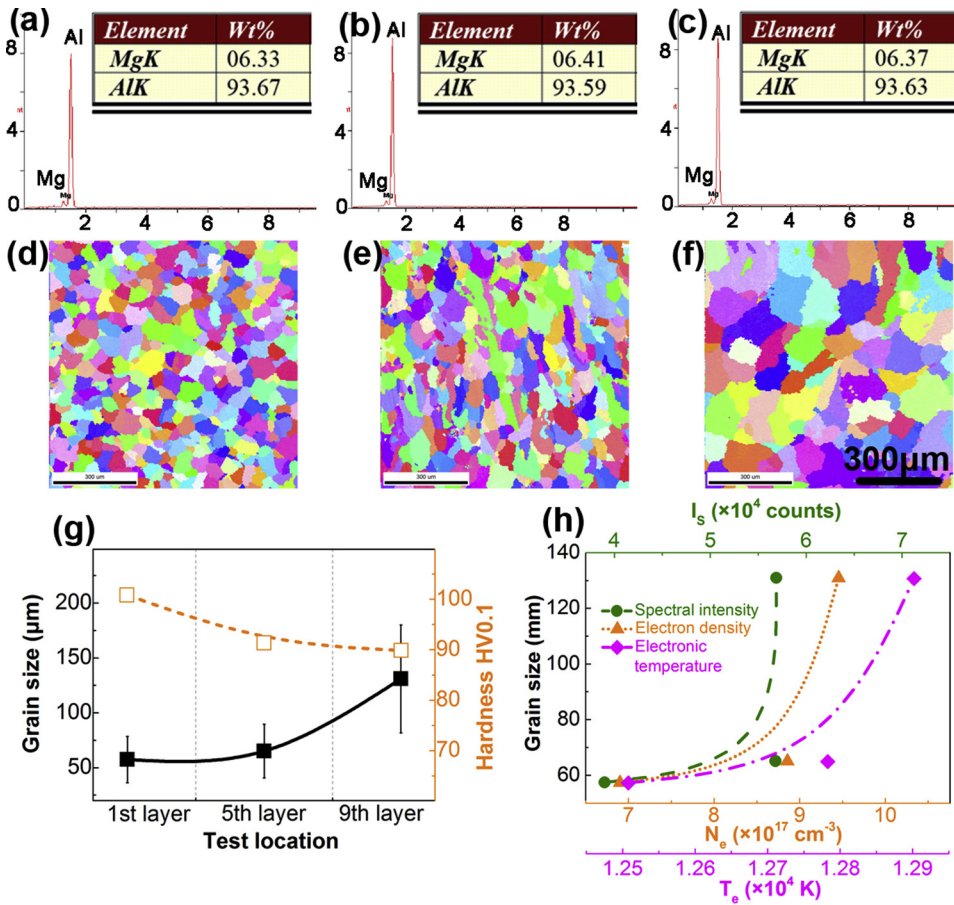


Fig. 6. Relationship between the arc characteristics and the microstructures of the deposited layers. EDS of the (a) first deposited layer, (b) fifth deposited layer, and (c) ninth deposited layer; EBSD inverse pole figure of the (d) first deposited layer, (e) fifth deposited layer, and (f) ninth deposited layer; (g) grain size and micro-hardness as functions of different deposited layers; (h) correlation between the arc characteristics and the grain size.

substrate in the initial deposited layer; however, the energy was concentrated in the upper deposited layer as shown in Fig. 4d and e, which could have also caused the grain size of the initial deposited layer to be smaller than that of the upper deposited layer. As a result, the absorbed energy of the cathode was not the only reason for the grain size variation. This indicates that the spectral diagnosis of the microstructures was not accurate.

### 3.4. Relationship between spectral characteristics of arc and porosity defects

Fig. 7 shows the metallographic images at the area pre-coated with the contaminants. More contaminants generated higher porosity and bigger pore sizes. The porosities in samples 5, 6, 7, and 8 were 0.48%, 0.53%, 1.61%, and 1.71%, respectively. All the pore sizes were less than 100 μm. Moreover, the distribution of the pores of all the samples was random. Fig. 7e shows the image of the X-ray CT for sample # 5

which contained several deposited layers. The total pore volume was 6.26 mm $^3$  and the total volume of the sample was 1230.68 mm $^3$ . Thus the percent porosity over the entire sample was about 0.5%, which was close to the porosity observed from the metallographic image. The pores were distributed evenly in the sample, which indicated that the porosity distribution shown by the local metallographic image of the cross section presented a true picture. Thus, it can be inferred that it is feasible to use metallographic images to calculate the porosity. Fig. 8a shows that the spectral intensities at the area pre-coated with the contaminant were higher than those in the other areas. The spectral intensity increased with the amount of contaminants. The maximum spectral intensities of the aforementioned samples were 236.3, 428.9, 1856, and 2731.8, respectively. The porosity as a function of the maximum spectral intensity is shown in Fig. 8b, which shows a linear correlation between the spectral intensity and the porosity.

The porosity during the fusion processing of Al alloys was caused by

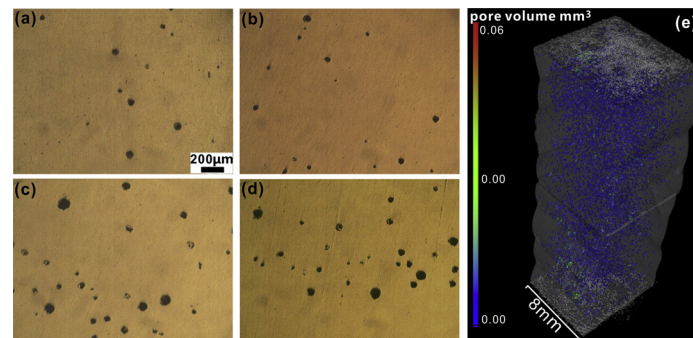


Fig. 7. Porosity in the metallographic images and the X-ray CT; (a) sample # 5 with 0 g of contaminant; (b) sample # 6 with 0.006 g of contaminant; (c) sample # 7 with 0.018 g of contaminant; (d) sample # 8 with 0.043 g of contaminant; (e) X-ray CT of sample # 5.

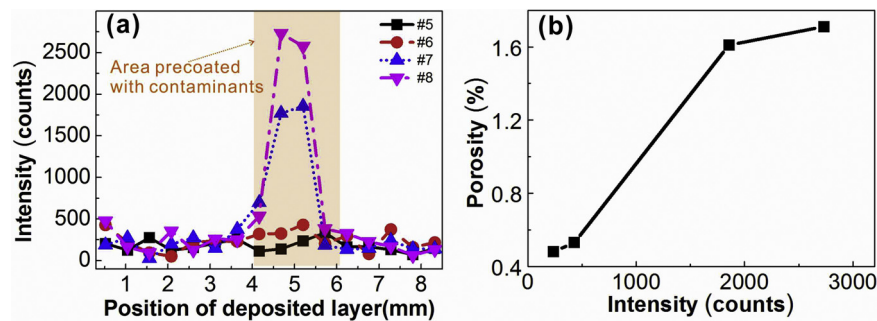


Fig. 8. (a) Spectral intensity in different positions of the pre-coated deposited layers; (b) porosity as a function of spectral intensity.

the contaminants. H was the dominant contaminant due to its contrasting solubility in solid and molten Al. The organic contaminants containing significant quantities of H melted into the molten pool during WAAM, which generated numerous pores. The more the contaminants were present, the higher the porosity. At the same time, as the contaminants were excited and ionized by the arc, the H spectral intensity was proportional to the porosity.

#### 4. Conclusion

Multiple-layered thin walls were manufactured by WAAM with the same parameters for each layer, and the arc was diagnosed by a spectrometer. Firstly, the forming width was analyzed. The arc characteristic parameters, namely the arc spectral intensity, electron density, and electron temperature of each deposited layer were calculated from the spectral lines. A good linear correlation between the spectral intensity/electron density and the width of deposited layer proved the feasibility of applying spectral diagnosis to WAAM. Secondly, the grain sizes of the upper, middle, and lower deposited layers in the WAAMed thin-wall were different. Nevertheless, it was proved that it was unlikely to be detected by spectral diagnosis, because not only the arc heat, but also the complex heat conducting environment influenced the solidification process. Finally, the porosity could be approximately detected by the spectral diagnosis of the arc characteristics owing to the close connection between the porosity and H, which was a dominant pollutant present in the system.

#### Declaration of Competing Interest

The authors declared that

#### Acknowledgments

This research is financially supported by the National Natural Science Foundation of China (Grant Nos. 51775206 and 51605343), the Natural Science Foundation of Hubei Province (Grant No. 2017CFB492) and the Fundamental Research Funds for the Central Universities (Grant No. 2042019kf0015).

#### References

- [1] B. Wu, Z. Pan, D. Ding, D. Cuiuri, H. Li, J. Xu, et al., A review of the wire arc additive manufacturing of metals: properties, defects and quality improvement, *J. Manuf. Process.* 35 (2018) 127–139.
- [2] K.S. Derekar, A review of wire arc additive manufacturing and advances in wire arc additive manufacturing of aluminium, *Mater Sci Tech-Lond.* 34 (2018) 895–916.
- [3] A.R. Nassar, J.S. Keist, E.W. Reutzel, T.J. Spurgeon, Intra-layer closed-loop control of build plan during directed energy additive manufacturing of Ti-6Al-4V, *Addit. Manuf.* 6 (2015) 39–52.
- [4] B.J. Simonds, J.W. Sowards, P.A. Williams, Laser-induced fluorescence applied to laser welding of austenitic stainless steel for dilute alloying element detection, *J. Phys. D Appl. Phys.* 50 (2017) 6.
- [5] A. Heralic, A.K. Christiansson, M. Ottosson, B. Lennartson, Increased stability in laser metal wire deposition through feedback from optical measurements, *Opt. Lasers Eng.* 48 (2010) 478–485.
- [6] C. Cunningham, J. Flynn, A. Shokrani, V. Dhokia, S. Newman, Invited review article: strategies and processes for high quality wire arc additive manufacturing, *Addit. Manuf.* 22 (2018) 672–686.
- [7] C. Zhang, Y. Li, M. Gao, X. Zeng, Wire arc additive manufacturing of Al-6Mg alloy using variable polarity cold metal transfer arc as power source, *Mater. Sci. Eng. A* 711 (2018) 415–423.
- [8] S.K. Everton, M. Hirsch, P. Stravroulakis, R.K. Leach, A.T. Clare, Review of in-situ process monitoring and in-situ metrology for metal additive manufacturing, *Mater. Des.* 95 (2016) 431–445.
- [9] M. Abdelrahman, E.W. Reutzel, A.R. Nassar, T.L. Starr, Flaw detection in powder bed fusion using optical imaging, *Addit. Manuf.* 15 (2017) 1–11.
- [10] Y. Zhang, J.Y.H. Fuh, D. Ye, G.S. Hong, In-situ monitoring of laser-based PBF via off-axis vision and image processing approaches, *Addit. Manuf.* 25 (2019) 263–274.
- [11] C. Gobert, E.W. Reutzel, J. Petrich, A.R. Nassar, S. Phoha, Application of supervised machine learning for defect detection during metallic powder bed fusion additive manufacturing using high resolution imaging, *Addit. Manuf.* 21 (2018) 517–528.
- [12] S. Clijsters, T. Craeghs, S. Buls, K. Kempen, J.-P. Kruth, In situ quality control of the selective laser melting process using a high-speed, real-time melt pool monitoring system, *Int. J. Adv. Manuf. Technol.* 75 (2014) 1089–1101.
- [13] T. Hua, C. Jing, L. Xin, Z. Fengying, H. Weidong, Research on molten pool temperature in the process of laser rapid forming, *J. Mater. Process. Tech.* 198 (2008) 454–462.
- [14] E. Rodriguez, F. Medina, D. Espalin, C. Terrazas, D. Muse, C. Henry, et al., Integration of a Thermal Imaging Feedback Control System in Electron Beam Melting, *Dissertations & Theses – Gradworks* (2013).
- [15] L. Song, V. Bagavath-Singh, B. Dutta, J. Mazumder, Control of melt pool temperature and deposition height during direct metal deposition process, *Int. J. Adv. Manuf. Technol.* 58 (2012) 247–256.
- [16] T. Watkins, H. Bilheux, K. An, A. Payzant, R. Dehoff, C. Duty, et al., Neutron characterization for additive manufacturing, *Adv Mater Process* 171 (2013) 23–27.
- [17] R. Cunningham, C. Zhao, N. Parab, C. Kantzos, J. Pauza, K. Fezzaa, et al., Keyhole threshold and morphology in laser melting revealed by ultrahigh-speed x-ray imaging, *Science* 363 (2019) 849–852.
- [18] M. Klein, J. Sears, Laser ultrasonic inspection of laser clad 316LSS and Ti-6-4, *Int. Congr. Appl. Lasers & Electro-Opt.* (2004) 1006.
- [19] J. Xiong, G. Zhang, Z. Qiu, Y. Li, Vision-sensing and bead width control of a single-bead multi-layer part: material and energy savings in GMAW-based rapid manufacturing, *J. Clean. Prod.* 41 (2013) 82–88.
- [20] G. Li, C. Zhang, M. Gao, X. Zeng, Role of arc mode in laser-metal active gas arc hybrid welding of mild steel, *Mater. Des.* 61 (2014) 239–250.
- [21] E. Hanova, Magnetic arc blow, *Weld. Int.* 5 (1991) 995–999.
- [22] M.B. Schwedersky, J.C. Dutra, S. RHGE, U. Reisgen, K. Willms, Double-electrode process speeds GTAW, *Weld. J.* 94 (2015) 64–67.
- [23] C.B. Stutzman, A.R. Nassar, E.W. Reutzel, Multi-sensor investigations of optical emissions and their relations to directed energy deposition processes and quality, *Addit. Manuf.* 21 (2018) 333–339.
- [24] P. Colombo, A.G. Demir, M. Norgia, B. Previtali, Self-mixing interferometry as a diagnostics tool for plasma characteristics in laser microdrilling, *Opt. Laser Eng.* 92 (2017) 17–28.
- [25] J. Mirapeix, A. Cobo, D.A. González, J.M. López-Higuera, Plasma spectroscopy analysis technique based on optimization algorithms and spectral synthesis for arc-welding quality assurance, *Opt. Express* 15 (2007) 1884–1897.
- [26] M. Gao, C. Chen, M. Hu, L. Guo, Z. Wang, X. Zeng, Characteristics of plasma plume in fiber laser welding of aluminum alloy, *Appl. Surf. Sci.* 326 (2015) 181–186.
- [27] S. Messaoud Aberkane, A. Bendib, K. Yahiaoui, S. Boudjemai, S. Abdelli-Messaci, T. Kerdja, et al., Correlation between Fe–V–C alloys surface hardness and plasma temperature via LIBS technique, *Appl. Surf. Sci.* 301 (2014) 225–229.
- [28] M.M. ElFaham, M. Okil, N.M. Nagy, Optical emission spectroscopy for concrete strength evaluation utilizing calcium lines, *Opt. Laser Technol.* 106 (2018) 69–75.
- [29] X.H. Zou, L.B. Guo, M. Shen, X.Y. Li, Z.Q. Hao, Q.D. Zeng, et al., Accuracy improvement of quantitative analysis in laser-induced breakdown spectroscopy using modified wavelet transform, *Opt. Express* 22 (2014) 10233–10238.
- [30] X. Hao, G. Song, Spectral analysis of the plasma in low-power Laser/Arc hybrid welding of magnesium alloy, *IEEE Trans. Plasma Sci. IEEE Nucl. Plasma Sci. Soc.* 37 (2008) 76–82.
- [31] H.R. Griem, *Plasma Spectroscopy*, New York: McGraw-Hill, 1964 1964;1.
- [32] J.A. Aguilera, C. Aragón, Characterization of a laser-induced plasma by spatially

- resolved spectroscopy of neutral atom and ion emissions: Comparison of local and spatially integrated measurements, *Spectrochim. Acta Part B At. Spectrosc.* 59 (2004) 1861–1876.
- [33] L.B. Guo, C.M. Li, W. Hu, Y.S. Zhou, B.Y. Zhang, Z.X. Cai, et al., Plasma confinement by hemispherical cavity in laser-induced breakdown spectroscopy, *Appl. Phys. Lett.* 98 (2011) 1459.
- [34] H.U. Eckert, *The Induction Arc: A State of the Art Review*, (1974).
- [35] V.D. Shafranov, O.G. Bakunin, M. Aksentieva, *Reviews of Plasma Physics*, Consultants Bureau, 1967.
- [36] Y. Kawahito, N. Matsumoto, M. Mizutani, S. Katayama, Characterisation of plasma induced during high power fibre laser welding of stainless steel, *Sci. Technol. Weld. Joi.* 13 (2008) 744–748.
- [37] V.N. Kolesnikov, Arc discharge in inert gases, *Trfizinstakadnauk Sssr.* 30 (1964).